Research Paper

Self-assembly of porphyrin-grafted lipid into nanoparticles encapsulating doxorubicin for synergistic chemo-photodynamic therapy and fluorescence imaging

Sadaf Hameed[1*], Pravin Bhattarai[1*], Xiaolong Liang[2*], Nisi Zhang[1], Yunxue Xu[1], Min Chen[1], Zhifei Dai[1✉]

1. Department of Biomedical Engineering, College of Engineering, Peking University, Beijing 100871, China
2. Department of Ultrasonography, Peking University Third Hospital, Beijing 100191, China

*These authors contributed equally to this work.

✉ Corresponding author: email: zhifei.dai@pku.edu.cn

Abstract

The limited clinical efficacy of monotherapies in the clinic has urged the development of novel combination platforms. Taking advantage of light-triggered photodynamic treatment combined together with the controlled release of nanomedicine, it has been possible to treat cancer without eliciting any adverse effects. However, the challenges imposed by limited drug loading capacity and complex synthesis process of organic nanoparticles (NPs) have seriously impeded advances in chemo-photodynamic combination therapy. In this experiment, we utilize our previously synthesized porphyrin-grafted lipid (PGL) NPs to load highly effective chemotherapeutic drug, doxorubicin (DOX) for synergistic chemo-photodynamic therapy.

Methods: A relatively simple and inexpensive rapid injection method was used to prepare porphyrin-grafted lipid (PGL) NPs. The self-assembled PGL NPs were used further to encapsulate DOX *via* a pH-gradient loading protocol. The self-assembled liposome-like PGL NPs having a hydrophilic core were optimized to load DOX at an encapsulation efficiency (EE) of ~99%. The resultant PGL-DOX NPs were intact, highly stable and importantly these NPs successfully escaped from the endo-lysosomal compartment after laser irradiation to release DOX in the cytosol. The therapeutic efficacy of the aforementioned formulation was validated both *in vitro* and *in vivo*.

Results: PGL-DOX NPs demonstrated excellent cellular uptake, chemo-photodynamic response, and fluorescence imaging ability in different cell lines. Under laser irradiation, cells treated with a low molar concentration of PGL-DOX NPs reduced cell viability significantly. Moreover, *in vivo* experiments conducted in a xenograft mouse model further demonstrated the excellent tumor accumulation capability of PGL-DOX NPs driven by the enhanced permeability and retention (EPR) effect. Through fluorescence imaging, the biodistribution of PGL-DOX NPs in tumor and major organs was also easily monitored in real time *in vivo*. The inherent ability of porphyrin to generate ROS under laser irradiation combined with the cytotoxic effect of the anticancer drug DOX significantly suppressed tumor growth *in vivo*.

Conclusion: In summary, the PGL-DOX NPs combined chemo-photodynamic nanoplatform may serve as a potential candidate for cancer theranostics.

Key words: porphyrin, doxorubicin, theranostics, chemotherapy, photodynamic therapy

Introduction

Annual global health statistics identify cancer among the leading causes of morbidity and mortality, thereby emphasizing the need to develop new effective anti-cancer therapies [1]. Among the various

burgeoning anti-cancer therapies, such as immunotherapy [2] and photothermal therapy [3], traditional chemotherapy still manifests as an effective frontline strategy. So far, anticancer drugs such as doxorubicin (DOX) that can inhibit the biosynthesis of RNA and DNA have been routinely used in the clinic for many years [4, 5]. However, DOX and other small-molecules share similar disadvantages when used directly *in vivo*: short blood circulation time, life-threating cardiotoxicity, and multi-drug resistance after repeated exposure [6, 7]. To overcome these limitations, attention has been directed towards the combination of multiple therapies, especially chemotherapy and phototherapy, which can yield a satisfactory therapeutic effect [8, 9].

In recent years, photodynamic therapy (PDT), having well-defined properties such as minimally invasive selective killing of cancer cells, eradication of deep-suited tumors without recurrence, and excellent biocompatibility, has emerged as a relatively safe method for the treatment of cancer [10-12]. In brief, PDT is driven by the activation of photosensitizers (PS) upon illumination by light of an appropriate wavelength, followed by transfer of excitation energy to molecular oxygen and the generation of cytotoxic reactive oxygen species (ROS) for effective tumor inhibition at the targeted site [13]. The efficacy of PDT usually depends on the choice and concentration of PS, oxygen enriched tumor microenvironment, irradiation dose, and the type of ROS generated [14, 15]. PSs from the porphyrin and chlorin families have been most studied and implemented in clinical trials [16]. They offer numerous advantages in serving both as a therapeutic and bio-imaging agent for PDT and *in vivo* fluorescence imaging, respectively [17]. For instance, they can enable (1) visualization of the targeted tumor zone, thus (2) confirming the level of PS uptake as well as accumulation within cancer tissues, and (3) allow continuous monitoring of the treatment response [18, 19]. In contrast, depending upon their molecular conformation, porphyrins can also be used as photothermal agents. Lovell et al. previously reported a liposome-like self-assembled structure called 'porphysome' made of phospholipid-porphyrin conjugates [20]. The high loading capacity of porphyrin in porphysome led to a highly quenched molecular conformation resulting in appreciable heat generation and subsequent photothermal ablation of tumors after irradiation with NIR laser. However, monotherapy alone (either PDT or PTT or chemotherapy) is insufficient to ablate tumors completely and is mostly accompanied by recurrence of the tumor several days after treatment. To this end, a combination model such as chemo-photodynamic therapy manifests great potential to overcome the limitations of monotherapy [21].

Chemo-photodynamic therapy provides a potential solution against tumor heterogeneity and drug resistance by initiating multiple mechanisms to fight cancer. Such synergistic effect can only be achieved by the co-delivery of chemotherapeutic drug and PS in the tumor region *via* a nanoscale drug delivery system (nDDS) such as hydrogel [22], nanofibers [23], liposomes [24] and micelles [25]. For instance, a nanoscale coordinated copolymer (NCPs) was designed to entrap Ce6 and DOX in a single nanoplatform. Upon light exposure, the resultant NCPs-DOX-Ce6 PEG NPs triggered simultaneous release of entrapped drug and PDT *via* generation of singlet oxygen for synergistic chemo-photodynamic therapy [26, 27]. Several other similar examples of synergistic combination therapy using various chemotherapeutic anticancer drugs and phototherapeutic modules with improved combined therapeutic effect have been reported recently [28, 29]. However, substantial aggregation accompanied by the compromised biological stability of nanocarriers at a higher loading content of porphyrin has seriously impeded the efficacy of PDT. In addition, such nanosystems remain quenched at high loading contents of porphyrin and therefore exert minimal PDT due to de-excitation of absorbed light energy *via* nonradiative pathways observed by the generation of heat.

Herein, we utilize our previously reported porphyrin-grafted lipids (PGLs) to further design an excellent combination nanoplatform for synergistic chemo-photodynamic therapy. In the previous work, Liang et al. successfully synthesized porphyrin-organoalkoxysilylated lipids (PORSILs) to form porphyrin bilayer cerasomes (PBCs) *via* a simple self-assembly mechanism [30]. The self-assembled PBCs showed excellent singlet oxygen generation, reasonable fluorescence signal and subsequent killing of tumor cells compared to free porphyrin. Motivated by this rationale, herein we propose a multifunctional PGL-based nanocarrier encapsulating hydrophilic DOX (PGL-DOX NPs) for fluorescence imaging-guided synergistic chemo-photodynamic therapy. A simple and inexpensive rapid injection method followed by optimization of the ratio of DOX to PGL yielded self-assembled NPs having high porphyrin and DOX content. Moreover, owing to efficient internalization of the NPs and laser-triggered ROS generation, potent *in vitro* efficacy against different tumor cell lines was also realized through chemo-photodynamic dual therapy. The *in vivo* tumor suppression effect of PGL-DOX NP was further

confirmed in a subcutaneous xenograft mouse model. In brief, PGL-DOX NP is aggregation-free even at a very high loading of PGL, provides reasonable fluorescence signal even in its intact form, prevents premature porphyrin release due to conjugation of porphyrin to the lipids, offers a large vesicle compartment for high loading of hydrophilic drugs, e.g., DOX, has a good circulation half-life *in vivo*, shows no thermal damage, and has excellent singlet oxygen generation ability and photocytotoxicity at a relatively low porphyrin concentration. The synergistic effect of PGL-DOX NPs towards inhibition of tumor growth *in vivo* underscores the superiority of nanomedicine and combination therapy in cancer theranostics compared to monotherapies.

Methods

Materials

PGL was synthesized using our already reported experimental protocol [30]. 1,2-distearoyl-sn-glycero-3-phosphoethanolamine-N-[methoxy (polyethylene glycol)-2000] (DSPE-PEG$_{2k}$; Mw, 2805.5), cholesterol (Mw, 386.65) and dipalmitoyl-sn-glycero-3-phosphocholine (DSPC; Mw, 790.2) were purchased from Shanghai A.V.T pharmaceutical Co. Ltd. (China). All other organic reagents such as chloroform and ethanol were purchased from Beijing Chemical (Beijing, China) and were of analytical grade. Roswell Park Memorial Institute (RPMI-1640) cell culture medium, penicillin, streptomycin, fetal bovine serum (FBS), and Trypsin-EDTA (0.25%) were purchased from Thermo Fisher Scientific. Singlet oxygen sensor green (SOSG), Calcein-AM, propidium iodide (PI), and methyl thiazolyl tetrazolium (MTT) were supplied by KeyGEN (Nanjing, China). All other chemicals not mentioned here were used without further purification. Ultrapure water produced by a Mili-Q-purification system (resistivity, 18.2 MΩcm^{-1}) was used in all experiments.

Synthesis of PGL NPs

PGL NPs were prepared through a rapid injection method. In this study, the finalized PGL NPs formulation was DSPC:cholesterol:PGL:DSPE-PEG$_{2k}$ = 52:33:10:5 mol%. Briefly, to synthesize 1.5 mL of PGL nanocarriers (0.83 µg/mL), the lipids and cholesterol were dissolved in ethanol at 60 °C, followed by rapid injection in 300 mM citrate buffer (pH 4) at 60 °C under continuous sonication.

Synthesis of PGL-DOX NPs

Encapsulation of DOX into PGL NPs (PGL-DOX NPs) was achieved by using a pH-gradient loading protocol as demonstrated by Mayer et al. [31] with a slight modification: sodium carbonate solution (500 mM) was used to adjust the exterior pH of the PGL NPs to 7.4, thus creating a pH-gradient (acidic inside PGL core). DOX with varying drug to lipid molar ratios (1:10, 1:15, 1:20, 1:25) was injected into the PGL nanocarriers solution under ultrasonic water bath at a temperature of 40 °C. The resultant PGL-DOX NPs were incubated at 37 °C overnight. Unencapsulated DOX from PGL-DOX nanoformulation was separated by centrifugation at 2191 ×g in an ultrafiltration tube (MW cut-off, 100,000 Da) for 10 min. PGL-DOX NPs stayed above the ultrafiltration membrane while free DOX was collected in the filtrate. Obtained PGL-DOX NPs were stored at 4 °C until further use.

Characterization of PGL-DOX NPs

90Plus/BI-MAS DLS analyser (Brookhaven Zeta PALS instruments) was utilized to obtain the values for the zeta-potential and hydrodynamic diameter of PGL-DOX NPs. UV-vis absorption spectra of PGL-DOX NPs were acquired using a UV-visible spectrophotometer (Evolution 220), while fluorescence measurements were obtained on a Lumina Spectrophotometer (Thermo Fisher Scientific). The morphology and size distribution of PGL-DOX NPs were determined by transmission electron microscopy (TEM, Hitachi, H-7650).

Drug loading efficiency and drug loading content

The content of DOX encapsulated in PGL-DOX NPs was evaluated by fluorescence spectrophotometry at Ex/Em: 480/590 nm. Briefly, freshly prepared PGL-DOX NPs were suspended in water and stirred for 10 min. The fluorescence intensity of DOX solution was measured and the amount of encapsulated DOX was evaluated using a linear calibration curve. Drug loading efficiency (DLE%) and drug loading content (DLC%) were calculated according to the following equations:

$$DLE\% = (W_{DOX} \text{ in PGL-DOX NPs}) / (W_{DOX} \text{ used initially}) \times 100\%$$

$$DLC\% = (W_{DOX} \text{ in PGL-DOX NPs}) / (W_{PGL-DOX NPs}) \times 100\%$$

where, W_{DOX} is the weight of DOX and $W_{PGL-DOX NPs}$ is the total amount of NPs in the solution.

DOX release profile *in vitro*

The *in vitro* release profile of chemotherapeutic drug (DOX) from PGL-DOX NPs was investigated by a simple dialysis method. Briefly, 1 mL of PGL-DOX NPs (0.05 mg/mL) was dispersed in water, transferred into a dialysis bag (MW cut-off, 8000-14000 Da, Viacase, American), immersed in 20 mL of PBS having pH values of 7.4 or 5 (mimicking

the acidic tumor microenvironment), and stirred gently at 160 rpm (37 °C). At predetermined time-points, 1 mL of PBS was withdrawn, and an equal PBS volume was added to keep the volume constant. The amount of released DOX in the PBS solution was detected by fluorescence spectrophotometry at Ex/Em: 480/590 nm. All experiments were carried out in triplicate.

Singlet oxygen generation in aqueous solution

Singlet oxygen generation by PGL-DOX NPs was monitored using SOSG probe. 10 μL of SOSG (0.5×10^{-3} M) and 5 μL of PGL-DOX NPs (with different sample concentrations to observe the effect of concentration on singlet oxygen generation) were mixed with 85 μL of H_2O in 96-well plates. Wells containing blank, PGL NPs, and PGL-DOX NPs were irradiated with a 650 nm laser for indicated times and SOSG fluorescence intensity was measured at Ex/Em: 490/520 nm using a microplate reader (BioTek Synergy HT).

Cellular uptake of PGL-DOX NPs

For *in vitro* studies, HeLa, and PC3 cell lines were used. The cells were cultured in RPMI 1640 medium that was supplemented with 10% fetal bovine serum (FBS) and 1% penicillin/streptomycin in a humidified incubator at 37 °C with 5% CO_2.

In order to visualize the cellular uptake behaviour of PGL-DOX NPs, PC3 cells were cultured on cover-glass in 24-well plates at a density of 1×10^5 cells per well and left for 24 h until confluency. Subsequently, the culture medium was removed, and cells were rinsed twice with PBS. Fresh medium containing 10 μM free DOX and PGL-DOX NPs (10 μM DOX equivalence) were then added and incubated. After 0 h, 2 h, 4 h and 6 h of incubation, the cell-containing glass slides were rinsed twice with PBS buffer, fixed with 4% paraformaldehyde for 15 min at 4 °C and stained subsequently with 2 μg/mL Hoechst 33342, as per the standard protocol provided by the supplier. Cellular localization of DOX was observed by confocal laser scanning microscopy (CLSM, Zeiss LSM 410, Jena, Germany). For PGL-DOX NPs, PGL Ex/Em: 420/650-800 nm and DOX Ex/Em: 480/500-590 nm; for Hoechst 33322, Ex/Em: 405/440-470 nm.

To quantify cellular uptake of the NPs, HeLa cells were seeded at a density of 2.0×10^5 per well in 6-well plates for 24 h. Then, the cells were treated with PGL NPs and PGL-DOX NPs (5 μM of PGL equivalent) for 2 h, 4 h and 6 h. Subsequently, cells were washed with PBS, trypsinized and re-suspended in 500 μL of PBS for flow cytometric measurements. The cellular fluorescence intensity of PGL was investigated by flow cytometry (FACSAria IIII, BD) at an excitation wavelength of 405 nm.

Furthermore, to evaluate the effect of light irradiation on cellular localization, HeLa cells were treated with free DOX, PGL NPs and PGL-DOX NPs (with an equivalent concentration of 30 μM DOX and 10 μM PGL) for 6 h. Then, the media was carefully discarded and fresh media containing LysoTracker Green (100 μL of working solution) was added to each well. After incubation for 15 min, the treated cells were washed with PBS 3 times, followed by confocal imaging.

Detection of cellular singlet oxygen upon irradiation

In order to monitor intracellular singlet oxygen generation, HeLa cells were seeded at a density of 5×10^4 per well on 24-well plates for 24 h. Then, HeLa cells were further incubated with PBS, PGL NPs and PGL-DOX NPs (concentration PGL, 5 μM). After 12 h, media containing drug sample was removed, cells were washed with PBS three times, followed by addition of serum-free 1640 RPMI medium containing SOSG (50 μM). After 1 h of incubation, cells were irradiated with 650 nm laser (0.2 W/cm^2, 10 min). Finally, media containing SOSG was replaced with 100 μL PBS and intracellular fluorescence of PGL (Ex/Em: 420/650 nm) and SOSG (Ex/Em: 490/530 nm) was monitored by a Leica DM 13000B (Wetzlar, Germany) fluorescence microscope at a magnification of 400.

In vitro chemo-photodynamic cytotoxicity

The cytotoxicity of PGL-DOX NPs against HeLa cells was evaluated by MTT assay. Briefly, HeLa cells were cultured in 96-well plates at a density of 1×10^5 cells per well. After 24 h, medium containing dead cells was removed, cells were washed with PBS, and fresh medium containing serial dilutions of free DOX (0.05-1.61 μM), PGL NPs (0.035-1.11 μM), and PGL-DOX NPs (equivalent to free DOX and PGL concentration) or only medium (control group) was added. After 24 h and 48 h of incubation, plates were irradiated with 650 nm laser (0.2 W/cm^2, 10 min). After 12 h of extra incubation in the dark, the chemo-photodynamic cytotoxicity was evaluated by MTT assay. Moreover, in order to evaluate possible synergy between DOX and PGL, combination index (CI) values were calculated using Compusyn software based on the Chou-Talalay combination index method. For this analysis, Drug 1 (DOX) was combined with Drug 2 (PGL) at a constant ratio determined by IC_{50} of DOX / IC_{50} of PGL. We entered the resulting data, along with the data obtained from single drug treatments, into

Compusyn software to obtain a CI value for each combination point, which quantitatively evaluates the additive, synergistic or antagonistic effects between DOX and PGL. The resulting values were utilized to plot a graph of CI values over a range of fractions affected.

Efficacy of chemo-photodynamic therapy by visual observation

For co-staining of live and dead cells, HeLa cells pre-seeded onto 24-well plates (5×10^4 cells per well) were incubated with PGL NPs and PGL-DOX NPs (equivalent PGL concentration 5 µM) for 24 h followed by laser treatment with a 650 nm laser (0.2 W/cm², 10 min). Cells were co-stained with PI/Calcein-AM (5 µM PI, 10 µM Calcein-AM) for 10 min at 37 °C. After 30 min of incubation, HeLa cells containing Calcein-AM/PI were washed twice with PBS and imaged with a fluorescence microscope for PI (Ex/Em: 530/620 nm) and Calcein-AM (Ex/Em: 488/520 nm).

The apoptotic and necrotic cell distributions were observed as per the instructions of the manufacturer using the Annexin V-FITC/PI Apoptosis Detection Kit. Briefly, HeLa cells at a density of 1.5×10^5 cells per well were seeded on 6-well plates, and allowed to attach for 24 h. Five groups were prepared in fi ve separate 6-well plates in triplicates: (i) control, (ii) PGL NPs without laser, (iii) PGL NPs with laser, (iv) PGL-DOX NPs without laser, and (v) PGL-DOX NPs with laser irradiation. The cells of groups (ii) and (iii) were co-incubated with PGL NPs (equivalent PGL, 5 µM) and cells of groups (iv) and (v) were co-incubated with PGL-DOX NPs (equivalent PGL 5 µM, DOX 5 µM) for 12 h while the control was only refreshed with fresh medium. After 12 h of incubation, the media of group (iii) and group (v) were replaced with fresh culture medium and cells were irradiated at 650 nm (0.2 W/cm²,10 min). All three groups were incubated for another 12 h. After incubation, HeLa cells were trypsinized, centrifuged for 4 min [129 ×g], rinsed with 2 × PBS and re-suspended in 200 µL of binding buffer. Finally, cells suspended in binding buffer were co-stained with 5 µL Annexin V-FITC and 5 µL PI solution for 15 min under dark conditions. Within 30 min, 300 µL of binding buffer was then added to each sample before the cells were assayed by flow cytometry (FACSAria, III, BD). The data were further analysed and reported by FlowJo 7.6 software.

Tumor model establishment

4-week-old female BALB/c nude mice were handled in accordance with a protocol approved by the Institutional Animal Care and Use Committee of Peking University. 4T1 murine breast cancer cells (1×10^7 in 80 µL PBS) were injected subcutaneously into the right hind leg of the mice under anaesthesia. The tumors reached a volume of approximately 100-200 mm³ within 5 days and were used for the biodistribution and pharmacodynamics studies.

Pharmacokinetics and biodistribution

PBS, PGL NPs, and PGL-DOX NPs were injected into tumor-bearing mice via tail vein at a dose of DOX: 5 mg/kg, PGL: 4.7 mg/kg and fluorescence images were captured at designated time-points (0, 4, 12, 24 h) using IVISTM-200 (Xenogen Corp). During the imaging process, the mice were anesthetized by isoflurane gas in oxygen flow. At 24 h post-injection, the mice were sacrificed and the tumor and main organs (heart, liver, spleen, lung, and kidney) were excised for *ex vivo* imaging and semi-quantitative biodistribution of PGL-DOX NPs.

To investigate the blood clearance rate of PGL NPs, 6-week-old female BALB/c mice (body weight 20-23 g) were i.v. injected 100 µL of PGL NPs solution (10 mg/kg). At pre-determined time intervals, blood samples were collected from the orbital venous plexus with heparin-coated capillary tubes. The plasma of the blood samples were collected after centrifugation at 716 ×g for 10 min. The porphyrin content in the plasma was determined by measuring the fluorescence intensity of porphyrin at 650 nm by microplate reader. A pharmacokinetic analysis using Origin (9.1) was performed to investigate the key parameters including elimination half-life ($t_{1/2}$) and area under the plasma concentration–time curve from 0 to 24 h (AUC_{0-24}) by fitting the curve with an ExpDec1 exponential function.

In vivo chemo-photodynamic combination therapy

Thirty BALB/c nude mice with an average tumor volume of 200 mm³ were selected and randomly divided into five groups. Each group received a different treatment: (i) PBS group injected with PBS; (ii) PBS/laser group injected with PBS and exposed to laser light; (iii) free DOX group treated with free DOX (5 mg/kg) without laser; (iv) PGL NPs/laser group treated with PGL NPs (4.7 mg/kg) and laser; (v) PGL-DOX NPs/laser group treated with PGL-DOX NPs (PGL: 4.7 mg/kg, DOX: 5 mg/kg) and laser. Aliquots (0.1 mL) of the freshly prepared NPs were injected intravenously into the mice only once throughout the *in vivo* experiment. The mice were kept in the dark except groups (ii), (iv), and (v) which were irradiated with a 650 nm laser at an irradiance of 0.2 W/cm² for 30 min. After the treatment, the tumor diameters were measured with a calliper in two

perpendicular dimensions every day. Moreover, the body weight was also recorded every day to ensure the biocompatibility of each treatment. The first administration day was recorded as day 1. Tumor volume (V) was calculated according to the formula: length × width^2 / 2. The mice treated with PGL-DOX NPs were sacrificed on day 11 and tumors were excised for histopathological analysis.

Statistical analysis

All experimental data are expressed as mean ± standard deviation (SD). Statistical differences between experimental groups for both *in vitro* and *in vivo* results were analysed using one-way ANOVA in Origin® software and are indicated with a single asterisk (*) for $p < 0.05$ and a double asterisk (**) for $p < 0.01$. All experimental data are represented in triplicate unless otherwise mentioned.

Results and Discussion

Preparation of PGL-DOX NPs

Nanocarriers mimicking liposome-like structures (hydrophilic core and hydrophobic bilayer) are efficient systems for loading water soluble and insoluble drugs. In this work, previously synthesized PGL and phospholipids, e.g., DSPC, cholesterol, and DSPE-PEG$_{2k}$, were self-assembled to encapsulate a water-soluble chemotherapeutic drug, DOX, so as to yield PGL-DOX NPs. DOX was loaded into PGL NPs via a transmembrane pH-gradient method. First, a transmembrane gradient was established by injecting the PGL and phospholipids mixture in an acidic citrate buffer solution to yield PGL NPs with an acidic core. Second, a basic solution of sodium carbonate was added to increase the pH of the external solution and establish a proton gradient pointed outward. This led to efficient diffusion of DOX across the membrane, resulting in a high DOX loading. In addition, the encapsulated DOX becomes protonated in the acidic interior of PGL NPs and is therefore assumed to be less permeable, resulting in high retention in the core of the NPs (**Figure 1A**). Since the amount of lipid in the NPs is crucial for regulating DOX loading, the first set of experiments was performed to investigate the effect of lipid ratio on encapsulation of DOX inside PGL NPs. The molar ratios of DSPC/cholesterol/PGL/DSPE-PEG$_{2k}$ selected for the preparation of PGL NPs were 50:30:10:10, 50:35:10:5, and 52:33:10:5. The loading content of porphyrin in PGL NPs at these particular molar ratios was calculated to be 6.37%. The as-prepared PGL NPs were further loaded with DOX by the previously explained pH-gradient method at the drug to lipid weight ratio of 1:10. The EE of DOX in PGL NPs was assessed by a traditional fluorescence spectrophotometric method. As shown in **Table S1**, the ratio of lipids has a significant effect on DLC and EE. The NPs formulation prepared with a lipid ratio of 52:33:10:5 achieved high DOX loading (10%) with an EE of almost 99%. The high EE of PGL-DOX NPs can also be verified from the photographic image presented in **Figure S1**. To ensure excellent therapeutic benefit, PGL-DOX NPs with a molar ratio of 52:33:10:5 having high drug loading and EE was chosen for further studies. Next, we were also motivated to investigate the DLC and EE of DOX with the change in drug to lipid (DOX/lipid) ratio. Previously optimized PGL NPs (52:33:10:5) were loaded with DOX at DOX/lipid ratios of 1:10 to 1:25 to yield PGL-DOX NPs. As shown in **Table 1**, the EE of DOX increased with decreasing DOX/lipid ratio from 1:25 to 1:10. However, DLS data showed that DOX/lipid ratio had no significant effect on the hydrodynamic size of the NPs. Finally, after optimization, a DOX/lipid ratio of 1:10 was selected for further *in vitro* and *in vivo* studies. The optimal DLC and high EE at the given molar ratio would minimize the risk of adverse side effects of the PS and chemotherapeutic DOX.

Table 1. Effect of DOX/lipid ratio on PGL-DOX NPs.

DOX/lipid molar ratio	Lipid composition DSPC:Chol:PGL:DSPE-PEG$_{2k}$	Effective diameter (nm) ± SD	PDI	EE (%)
1:10	52:33:10:5	82.16 ± 6.71	0.151	~99
1:15	52:33:10:5	98.40 ± 8.53	0.153	~98
1:20	52:33:10:5	102.76 ± 8.79	0.169	~96
1:25	52:33:10:5	115.95 ± 9.95	0.158	~89

PGL: porphyrin-grafted lipid; PDI: polydispersity index; EE: encapsulation efficiency.

Characterization of PGL-DOX NPs

We then carefully characterized the as-synthesized PGL-DOX NPs. As measured by DLS, the as-prepared NPs showed a uniform size distribution with a mean diameter of ~82 nm (**Figure 1B**). Zeta-potential analysis further showed a negative surface charge of -12 mV for PGL-DOX NPs. TEM revealed that the obtained PGL-DOX-NPs have a uniform sphere-like morphology (**Figure 1C**). Moreover, the hydrodynamic diameter of PGL-DOX NPs in aqueous solution measured over a span of 5 weeks showed only slight fluctuation, suggesting good stability, without sedimentation or aggregation of the nanoformulations (**Figure S2**). The changes in optical properties of PGL NPs and PGL-DOX NPs were also investigated by fluorescence spectrophotometry and UV-vis spectrometry.
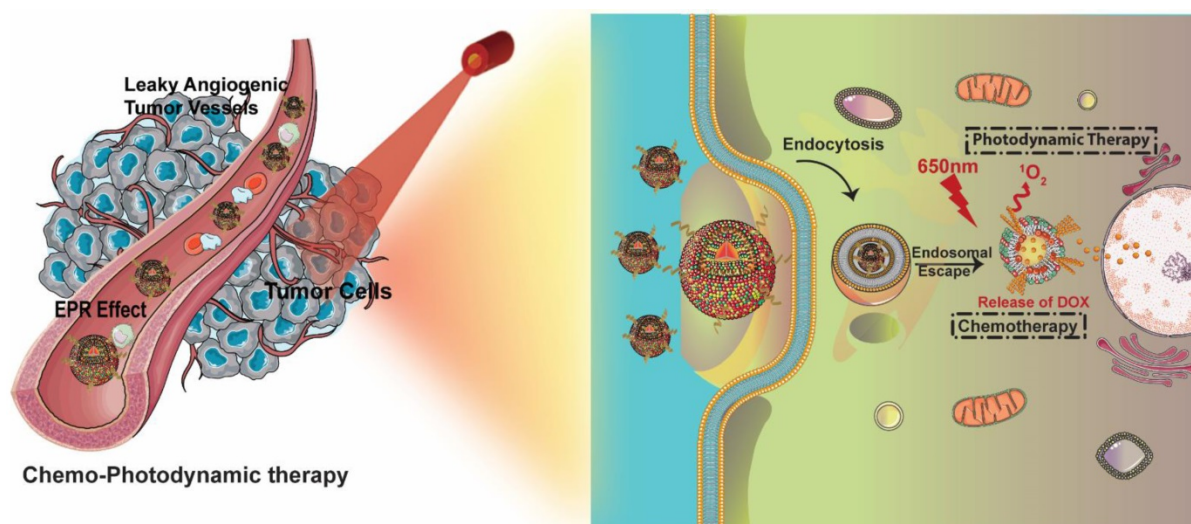
Scheme 1. Schematic representation of PGL-DOX NPs for chemo-photodynamic therapy. DOX: doxorubicin; EPR: enhanced permeation and retention; PGL: porphyrin-grafted lipids.
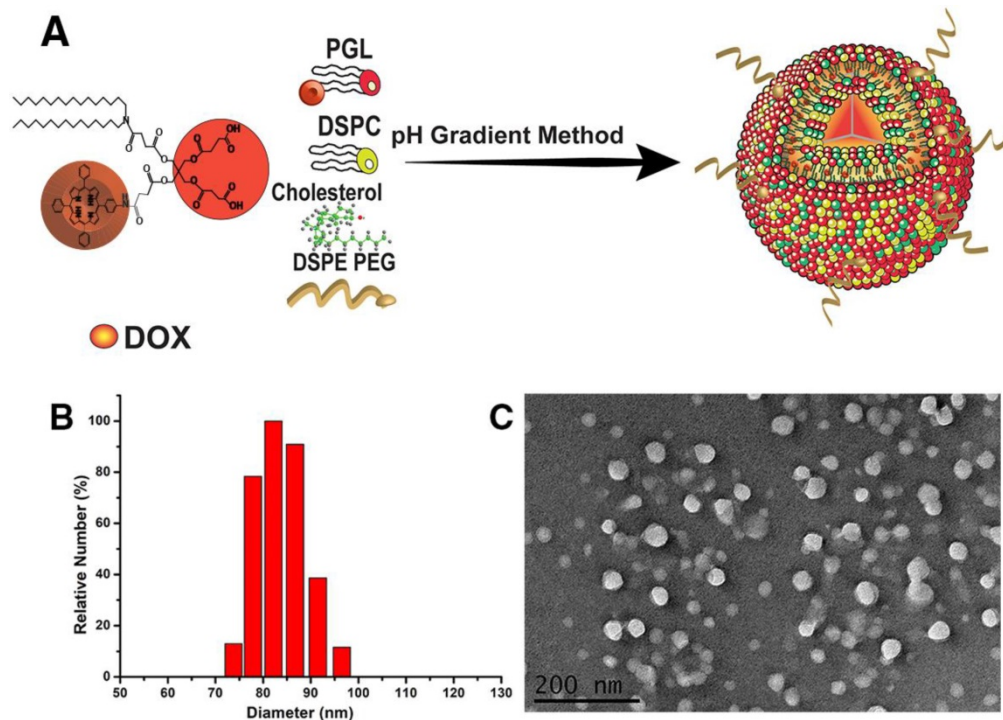

Figure 1. (A) Schematic representation of PGL-DOX NPs synthesis process. Characterizations of PGL-DOX NPs: **(B)** size distribution; **(C)** TEM micrograph.

A series of spectrophotometric experiments was performed with PGL-DOX NPs prepared at different DOX/lipid ratios, i.e., 1:10, 1:15, 1:20, 1:25. **Figure 2A** depicts the UV-vis absorption spectra of PGL-DOX NPs with different DOX/lipid ratios. A maximum absorption band for free porphyrin appears at 420 nm; however, a strong effect from DOX encapsulation can be seen in the visible region, where the absorption intensity of the Soret band at 420 nm decreases with an increase in the concentration of DOX in different PGL-DOX NPs formulations. This hypochromic effect

could be due to the combination of electrostatic binding forces in PGL-DOX NPs. This hypochromic effect at the absorption maximum of porphyrin is taken as evidence of interaction between DOX and PGL. In addition to the decrease of absorbance at 420 nm for porphyrin, a 4 nm shift of λ_{max} to a longer wavelength was also observed. This slight bathochromic shift is possibly due to π-π stacking interactions between DOX and PGL [32]. The fluorescence spectra of PGL NPs and PGL-DOX NPs were also recorded at an excitation wavelength of 420

nm for porphyrin and 480 nm for DOX. As shown in **Figure 2B-C**, upon excitation at 480 nm, the emission peak of PGL-DOX NPs appeared between 520-620 nm, consistent with free DOX. Moreover, increasing the DOX concentration in different DOX/lipid ratios correspondingly increased the fluorescence intensity. This data demonstrates the ability of DOX to retain its optical properties even after encapsulation in PGL NPs. Furthermore, the intensity of PGL in PGL-DOX NPs at 655 nm gradually decreased with increasing concentration of DOX. The change in the intensity might be due to the resonance energy transfer from PGL to DOX when packed closely inside the NP compartment.

DOX release profile *in vitro*

The release profile of DOX *in vitro* was carefully investigated in acidic (pH 5) and normal (pH 7.4) physiological conditions. Both free DOX (control) and DOX encapsulated in PGL NPs were dialysed against two different solutions under similar reaction conditions (at 37°C). As shown in **Figure 3**, free DOX

released completely (~100%) within the first 4 h, whereas PGL-DOX NPs showed a typical biphasic release profile in both acidic and normal physiological conditions. It was observed that the encapsulated DOX released relatively faster in the first few hours, followed by a sustained release for over 72 h. Moreover, the cumulative DOX release from PGL-DOX NPs accelerated when the pH value changed from 7.4 to 5. This is solely attributed to the fact that DOX has pH-dependent hydrophilicity [33]. Under neutral physiological conditions, the deprotonated DOX is hydrophobic and favours π-π stacking interactions with PGL, which is beneficial to avoid burst drug release in the blood stream. In contrast, the solubility of DOX increases at acidic pH conditions due to protonation of the daunosamine group, which no longer facilitates hydrophobic π-π stacking interactions between DOX and PGL [34]. Therefore, the pH-sensitive release of DOX from PGL-DOX NPs could be beneficial to achieve better therapeutic outcomes.
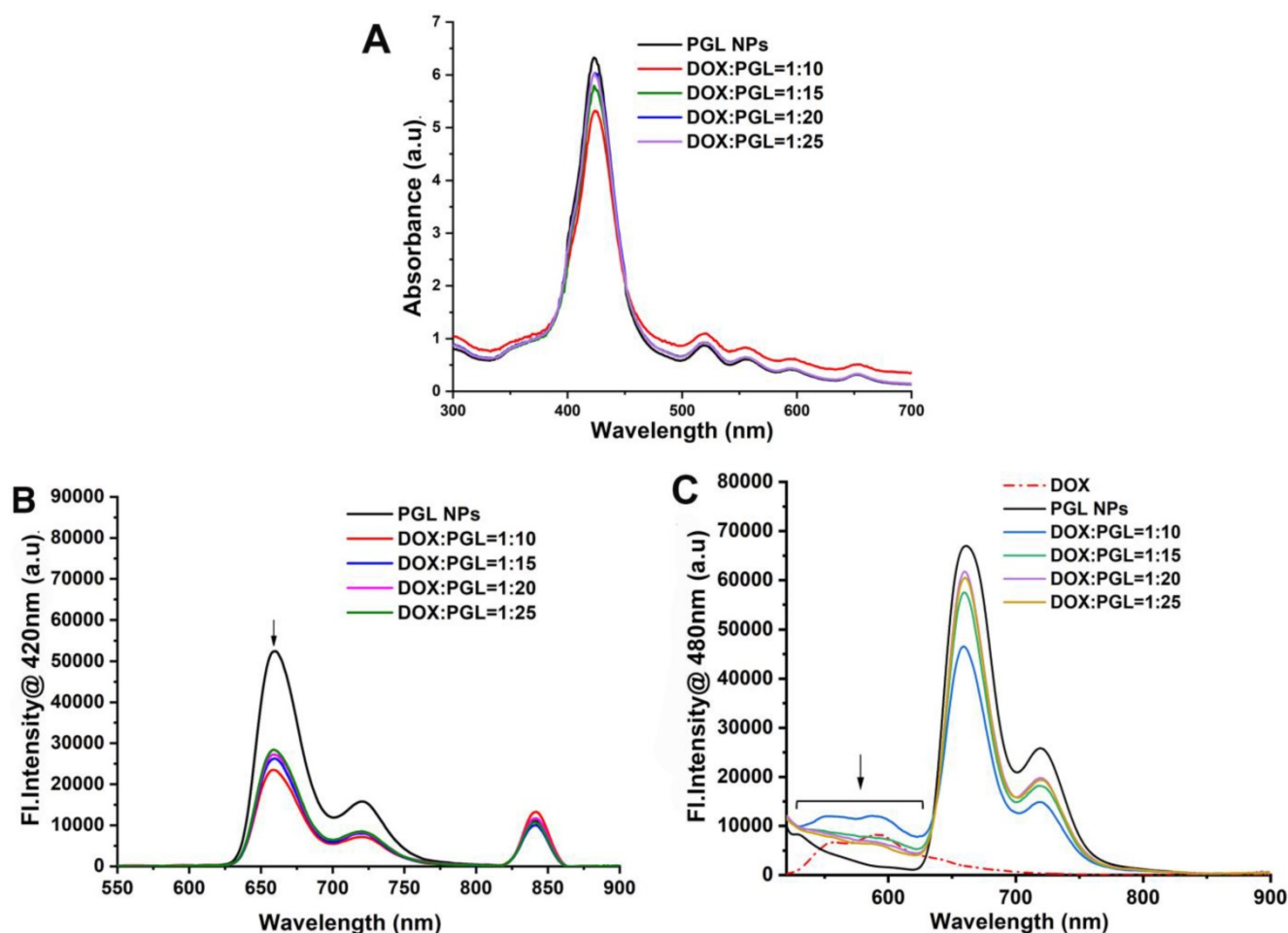

Figure 2. Spectroscopic measurements of PGL-DOX NPs with different molar ratios of DOX to lipid. **(A)** UV-vis absorption spectra showing characteristic absorption peaks of PGL and DOX. **(B)** Fluorescence spectra upon excitation at 420 nm. **(C)** Fluorescence spectra upon excitation at 480 nm.
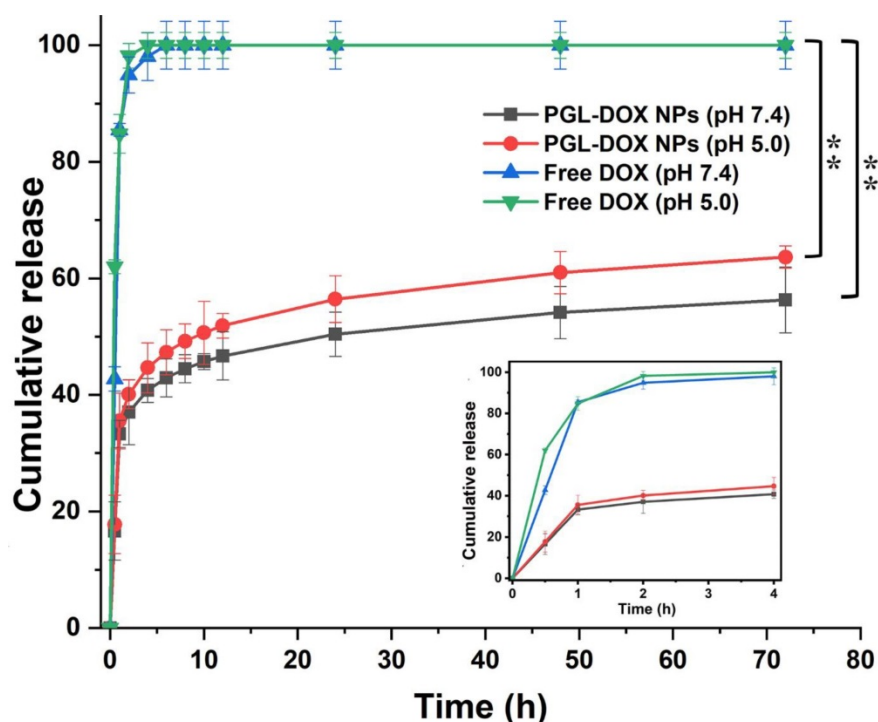
Figure 3. *In vitro* release profile of free DOX and DOX from PGL-DOX NPs at different pH values. Data are presented as mean ± SD (n=3), *$p < 0.05$, **$p < 0.01$. SD: standard deviation.

Investigation of singlet oxygen generation in aqueous solution

Apart from the controlled release of DOX, the excellent singlet oxygen generation ability of PGL-DOX NP is also a key parameter for combination therapy. Singlet oxygen is usually generated from PS during irradiation with laser light of an appropriate wavelength and is responsible for triggering cellular apoptosis and inducing cellular damage. To this end, we investigated the light-triggered singlet oxygen generation from PGL-DOX NPs indirectly using a fluorescent probe, singlet oxygen sensor green (SOSG). SOSG reacts with singlet oxygen generated during PDT to generate SOSG endoperoxides (SOSG-EP) that are fluorescent with excitation at 504 nm and emission at 525 nm. The relative SOSG intensity of PGL NPs and PGL-DOX NPs showed slightly different singlet generation ability *in vitro*. Despite the slight quenching effect, the production of singlet oxygen from PGL-DOX NPs was still comparable to PGL NPs under light irradiation (650 nm, 0.2 W/cm²) (**Figure 4A**). Furthermore, the singlet oxygen generation ability of PGL-DOX NPs against a series of PGL concentrations was also investigated. An obvious increase in the amount of singlet oxygen generation was observed for increasing PGL concentration from 0.1 μM to 3.47 μM. The increase in SOSG fluorescence after irradiation by 650 nm laser at different time intervals closely followed the increase

in concentration of PGL (**Figure 4B**). These results indicate that PGL-DOX NPs can generate sufficient singlet oxygen, when excited at an appropriate wavelength, for combination chemo-photodynamic therapy. Additionally, the PGL NPs and PGL-DOX NPs solutions (with an equivalent concentration of PGL, 3.47 μM) did not show any significant elevation in temperature upon irradiation by 650 nm laser (**Figure S3**), thus demonstrating the absence of thermal generation during the PDT process. Furthermore, in order to demonstrate that there is no interaction between the singlet oxygen and DOX, we irradiated DOX and DOX+PGL NPs solutions with 650 nm laser for 5 min and observed no discernible change in the absorption spectrum (**Figure S4A**). Moreover, relative absorbance analysis revealed negligible interference of singlet oxygen with DOX (**Figure S4B**). Notably, the corresponding decrease in the absorption peak of DOX was only due to the laser irradiation but not singlet oxygen.

Cellular uptake of PGL-DOX NPs

The delivery of therapeutic agents into the cytoplasm and nucleus is critical for successful cancer therapy. To explore their cellular uptake behaviour, cells incubated with PGL-DOX NPs for predetermined time intervals were imaged by CLSM. As depicted in **Figure 5A**, three types of fluorescence were observed: green for DOX, red for PGL and blue for Hoechst 33342. The fluorescence signals of DOX

were mainly observed in the nuclei, possibly due to the pH-induced release of DOX from the nanocarriers, whereas PGL red fluorescence generally accumulated in the cytoplasm of the tumor cells. We further prolonged the incubation time from 2 h to 6 h and observed remarkably increased fluorescence for both DOX and PGL. This suggests improved uptake of PGL-DOX NPs by tumor cells *in vitro*. Flow cytometry was further used to quantify the intracellular uptake behaviour of PGL NPs and PGL-DOX NPs (**Figure 5B**). Obvious enhancement in fluorescence intensity was observed after 2 h incubation, indicating

rapid uptake of PGL and PGL-DOX NPs by HeLa cells. Furthermore, the fluorescence intensity increased progressively with incubation time. After 6 h of incubation, the average fluorescence intensity of PGL-DOX NPs was nearly 47-fold greater than the control, while PGL NPs showed a 38-fold increase in fluorescence intensity (**Figure 5C**). Herein, both CLSM and flow cytometry results validate that PGL-DOX NPs are taken up effectively by tumor cells and can be used further for investigating therapeutic efficacy.
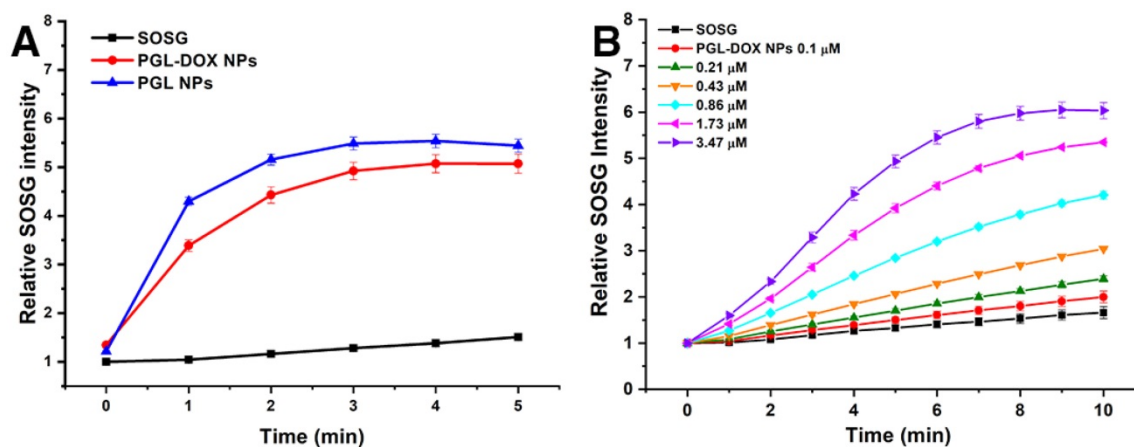

Figure 4. Detection of singlet oxygen in solution. **(A)** Time-dependent generation of SOSG fluorescence under light exposure (650 nm, 0.2 W/cm²) for PGL and PGL-DOX NPs at the same PGL concentration (1 μM). **(B)** PGL concentration-dependent (0.1-3.47 μM) recovery of SOSG fluorescence under light exposure (650 nm, 0.2 W/cm²) for 10 min. SOSG: singlet oxygen sensor green.
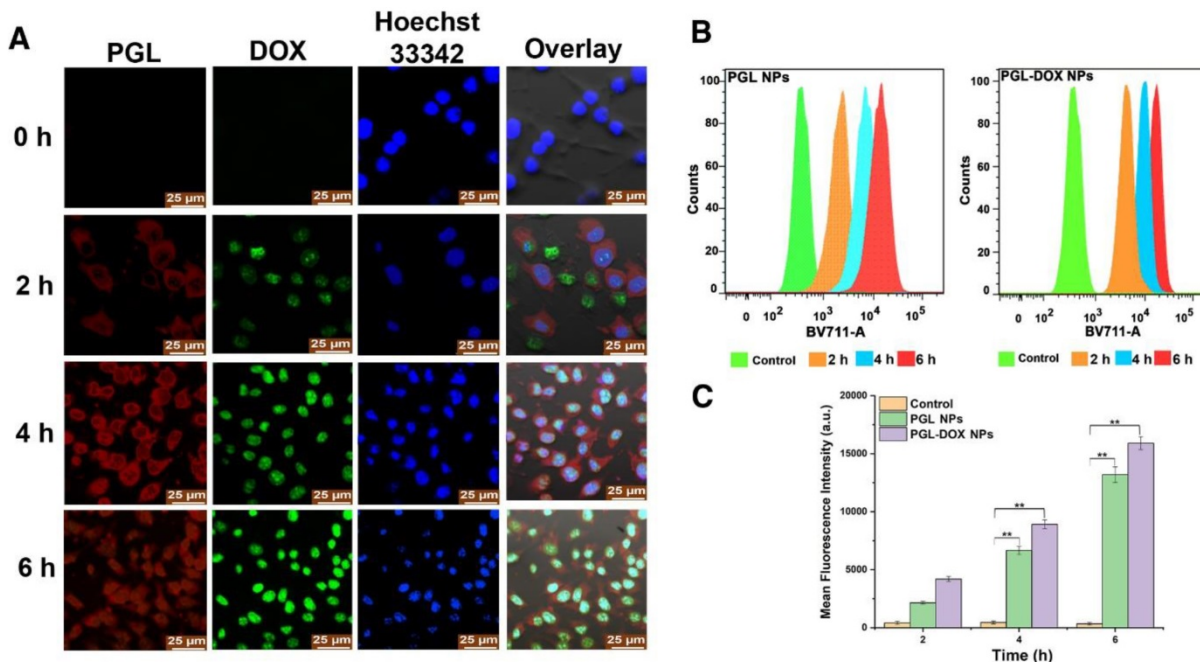

Figure 5. Intracellular uptake of PGL-DOX NPs. **(A)** Confocal microscopy images of HeLa cells incubated with PGL-DOX NPs for different time intervals with an equivalent DOX concentration of 1 μM. All images were acquired at the same magnification (scale bar, 25 μm). **(B-C)** Time-dependent quantitative analysis of fluorescence intensity of PGL NPs and PGL-DOX NPs in HeLa cells measured by flow cytometry.
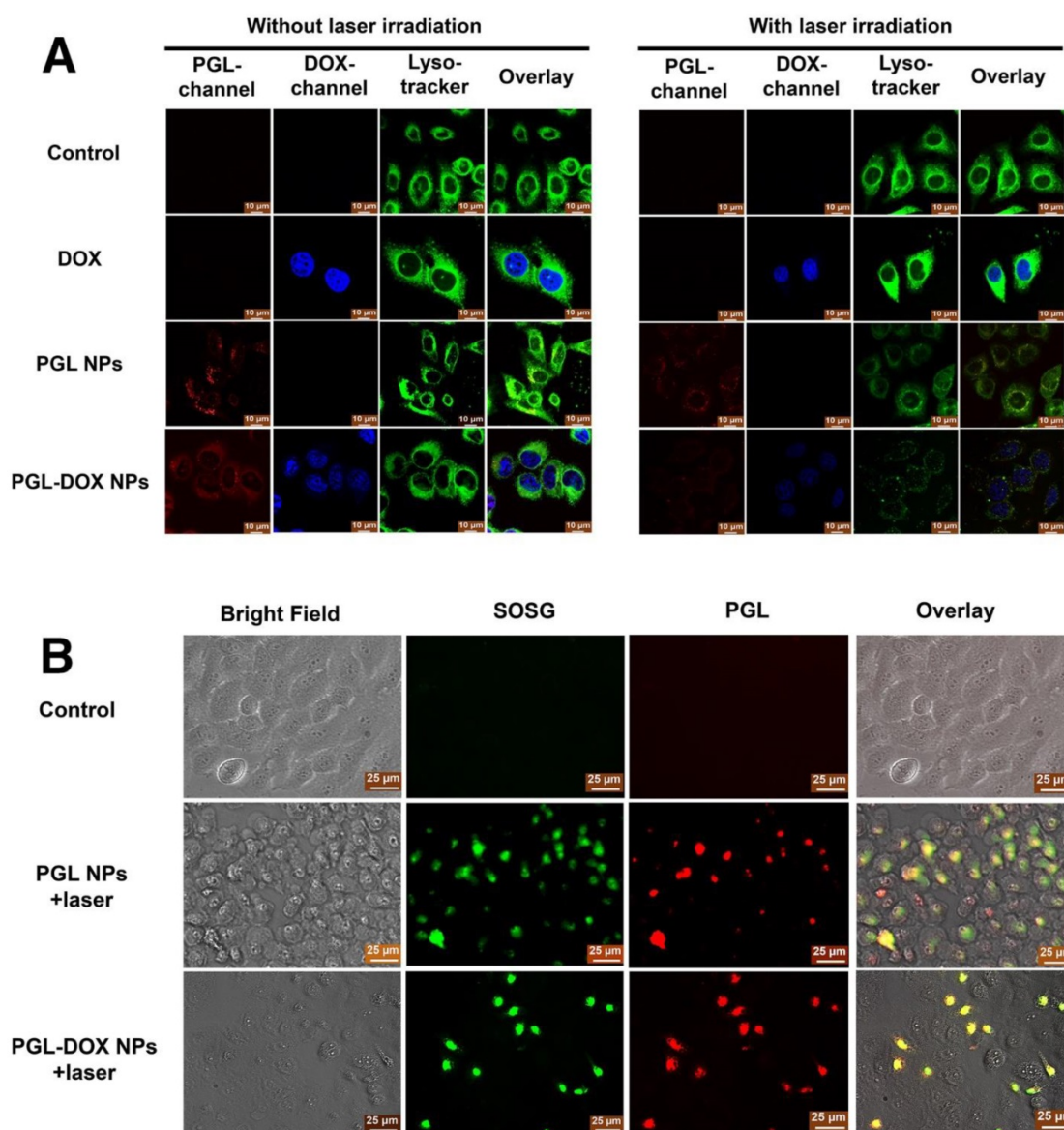
Figure 6. (A) Confocal microscopy analysis of cellular localization of PGL-DOX NPs in HeLa cells before and after laser irradiation (0.2 W/cm^2, 5 min; scale bar, 10 μm). **(B)** Detection of singlet oxygen in HeLa Cells. SOSG showed green fluorescence in the presence of singlet oxygen. The cellular uptake of PGL-DOX NPs was observed in the red channel, which showed the fluorescence of PGL (scale bar, 25 μm).

Light-triggered lysosomal escape of PGL-DOX NPs

To further track the intracellular distribution of PGL-DOX NPs before and after laser irradiation, HeLa cells were treated with PGL-DOX NPs followed by 650 nm laser irradiation (0.2 W/cm^2, 5 min). DOX and PGL could be tracked by their intrinsic fluorescence (coloured in blue and red respectively in **Figure 6A**). Additionally, cells were also incubated with LysoTracker Green (blue excitation, green emission, coloured in green in **Figure 6A**) in order to label lysosomal compartments. As shown in **Figure 6A**, an overlay of green (LysoTracker Green-stained lysosome), red (PGL) and blue (DOX) fluorescence revealed that the PGL-DOX NPs were successfully localized in lysosomes. We then explored the ability of PGL-DOX NPs to escape from the lysosomes by light irradiation. Light irradiation triggers PGL to generate highly oxidative singlet oxygen, which could efficiently damage lysosomal membranes and then induce lysosomal disruption for PGL-DOX NPs to escape into the cytoplasm. The fluorescence signal of lysotracker green reduced after irradiation (**Figure 6A**), indicating effective photodynamic disruption of the lysosomal structure. Both PGL and PGL-DOX NPs induced subsequent damage to lysosomes, as observed by the reduced green fluorescence intensity. More obvious damage to lysosomes was observed after laser irradiation, which is possibly due to the enhanced photodynamic effect of PGL-DOX NPs after

the DOX was released. In contrast, free DOX did not show any obvious disruption of lysosomes under the same irradiation condition, as demonstrated by the intense green fluorescence signals. As a result, it is clearly observed that the NPs can successfully escape to the cytoplasm of the cell after subsequent disruption of lysosomal structures in the presence of laser irradiation. Such observation is relevant to enhanced therapeutic efficacy, especially in a nanosystem designed for combination therapy such as PGL-DOX NPs.

Detection of cellular singlet oxygen upon irradiation

After successful observation of the extracellular singlet oxygen generation ability of PGL-DOX NPs, we employed an SOSG staining method to examine the intracellular singlet oxygen generation. To assess this, three different groups were prepared and examined separately: control (SOSG + 650 nm laser irradiation), PGL NPs (SOSG + 650 nm laser irradiation) and PGL-DOX NPs (SOSG + 650 nm irradiation). HeLa Cells were treated with PBS, PGL NPs, and PGL-DOX NPs, with 10 min continuous laser irradiation (650 nm laser). After laser irradiation, cells incubated with PGL and PGL-DOX NPs exhibited significant green fluorescence (**Figure 6B**), indicating that the NPs could be efficiently taken up by tumor cells and therefore generate sufficient singlet oxygen *in vitro* to afford effective photodynamic effect.

In vitro chemo-photodynamic cytotoxicity study

Subsequently, in order to evaluate the *in vitro* anti-tumor efficacy of the NPs, the cytotoxicity of different formulations with or without laser irradiation was investigated against two different cell lines (PC-3 and HeLa) by CCK-8 and MTT assays. The CCK-8 assay was executed to detect the potential dark cytotoxicity of PGL NPs and PGL-DOX NPs. As shown in **Figure 7A**, PGL NPs showed negligible cytotoxicity in the dark, even at a high concentration of 10 μM, while PGL-DOX NPs showed a similar degree of toxicity as free DOX to tumor cells without laser irradiation. Furthermore, to evaluate the *in vitro* anti-tumor efficacy of chemotherapy, PDT, and combination chemo-photodynamic therapy in HeLa cells, we performed MTT assay. Cell viability was measured as the percentage of the optical density (OD) of viable cells over the OD of untreated cells or control (i.e., without drug incubation and laser exposure). First, we examined cell viability for free DOX at two different time-points, i.e., 24 h and 48 h; as shown in **Figure 7B**, no significant cytotoxicity was observed in cells treated with free DOX at concentrations up to 1.61 μM. Moreover, no cell death was observed regardless of whether DOX-treated cells were irradiated with light or not. This is probably due to the inert nature of DOX towards the generation of singlet oxygen or toxic radicals. In contrast, HeLa cells treated with PGL NPs showed significant dose- and time-dependent phototoxic profiles upon light irradiation at 0.2 W/cm² for ~10 min, which could ensure the singlet oxygen generation ability of PGL to inhibit tumor cell proliferation effectively.

The combination chemo-photodynamic effect of PGL-DOX NPs was then investigated on cancer cells. HeLa cells were incubated with various concentrations of PGL-DOX NPs in combination with 10 min laser irradiation at 650 nm, 0.2 W/cm². Cell viability was evaluated after 24 h and 48 h incubation and showed that the cytotoxicity significantly increased with increasing concentration of PGL-DOX NPs and incubation time. The higher cytotoxicity of PGL-DOX NPs validates our presumption of increased cellular uptake with respect to time, enhanced DOX release in the intracellular acidic tumor environment and effective PDT after the release of DOX *in vitro*. This result indicates that the combination chemo-photodynamic therapy of PGL-DOX NPs could provide more effective cancer treatment than chemotherapy or PDT alone.

For combination cancer therapy, it is expected that the net effect of the two therapeutic moieties is synergistic or greater than the sum of the effects of each moiety alone. There are many formalisms to ensure synergy in such combination treatments; the combination index (CI) is considered the simplest method. CI is generally utilized to measure the synergistic effect between different therapies, and CI values of <1, 1, and >1 represent synergism, additive effect, and antagonism, respectively [35]. Herein, a CI < 0.4 was calculated for PGL-DOX NPs in HeLa cells (**Figure S5**), suggesting a strong synergistic effect of the combination chemo-photodynamic therapy.

Efficacy of chemo-photodynamic therapy by visual observation

Additionally, in order to evaluate whether the inhibition of cell proliferation by PGL NPs and PGL-DOX NPs plus laser was due to its apoptotic effect, a live-dead assay of HeLa cells following uptake of NPs with and without laser irradiation was performed. This assay was conducted according to the previously described protocol [36] by Calcein-AM/PI double staining. In the experiment, the two control groups with and without laser irradiation and PGL NPs without laser irradiation did not reveal any dead cells (PI, red), as seen in **Figure 7C**, but had almost all

live cells showing green fluorescence (Calcein-AM, green). This indicated that the effect of laser irradiation in the control and PGL groups was almost null. In comparison to the control and PGL (-laser) groups, PGL-DOX NPs without irradiation had slightly higher cell apoptosis, as depicted by few PI stains. This can be mainly due to the slow release of DOX at the time of therapy. After laser irradiation for 10 min, PGL NPs showed relatively higher cell death as observed in **Figure 7**C. In stark contrast, PGL-DOX

NPs irradiated by laser had more than 98% cell apoptosis (red) and no green fluorescence was obvious. The enhanced therapeutic killing of HeLa cells is mainly due to the strong ROS generation by PGL combined with the cytotoxic effect of DOX, which is pronounced after laser irradiation. These data also revealed that the inhibited cell proliferation induced by PGL-DOX NPs plus laser was at least partially attributed to its apoptotic effect.
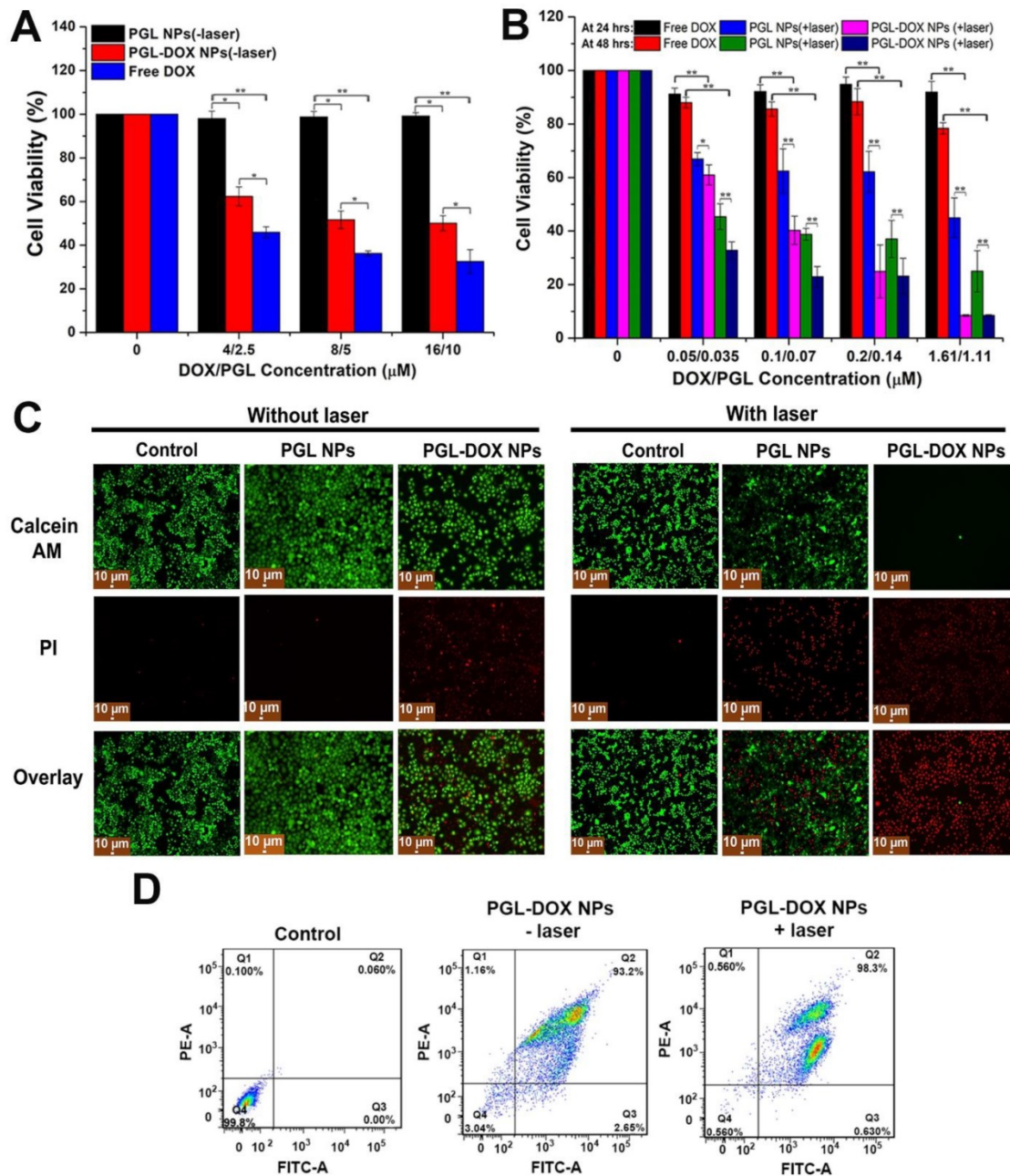

Figure 7. *In vitro* cell experiment in HeLa/PC3 cell lines incubated with various concentrations of PGL-DOX NPs. **(A)** Cell viability assay of PC3 cells incubated with PGL-DOX NPs without irradiation at a PGL concentration range of 0-10 μM and DOX concentration range of 0-16 μM. **(B)** Cell viability assay of HeLa cells incubated with different concentrations of PGL-DOX NPs with irradiation for 10 min. **(C)** Fluorescence microscopy images of HeLa cells stained with Calcein-AM and PI after treatment with PGL NPs and PGL-DOX NPs in the presence and absence of laser. Live HeLa cells are represented with green colour (Calcein-AM) and dead cells are represented with red colour (PI). Scale bar, 10 μm. **(D)** Flow cytometry analysis of tumor cells apoptosis induced by PGL-DOX NPs with and without laser irradiation based on Annexin V-FITC/PI staining. The values in (A-B) are presented as mean ± SD, *$p < 0.05$, **$p < 0.01$.

Furthermore, Annexin V-FITC/PI apoptosis assay reconfirmed the apoptosis and necrosis-inducing capabilities of PGL NPs and PGL-DOX NPs with and without laser irradiation. Minimal apoptosis and necrosis of HeLa cells (<20%) was induced by PGL NPs without laser irradiation, which increased to nearly 50% in the presence of laser (**Figure S6**). Meanwhile, incubation of tumor cells with PGL-DOX NPs for 24 h resulted in almost 93% apoptotic cells and only 2% necrotic cells. In contrast, tumor cells when exposed to PGL-DOX NPs followed by irradiation with 650 nm light showed a different apoptotic behaviour with a high late apoptotic ratio of almost 98% (**Figure 7D**). The flow cytometry results revealed that early and late apoptosis are the major death modes of HeLa cells, which was caused by the synergistic effect of DOX and PGL in PGL-DOX NPs-mediated chemo-photodynamic therapy.

In brief, PGL-DOX NPs exhibited good biocompatibility, enhanced cellular uptake, sustained release of DOX, effective ROS generation and significant inhibition and proliferation of cancer cells growth. Based on these findings, we were convinced to evaluate the therapeutic efficacy of PGL-DOX NPs *in vivo*.

Pharmacokinetics and biodistribution

A fluorescence imaging approach was adopted to detect the biodistribution and tumor accumulation of PGL NPs and PGL-DOX NPs in 4T1 tumor-bearing female nude mice. PBS, PGL and PGL-DOX NPs were injected intravenously *via* tail-vein and the fluorescence intensity at the tumor site was observed until 24 h. **Figure 8A** shows the fluorescence signal of tumor sites in mice injected with PBS, PGL NPs and PGL-DOX NPs. In general, PGL NPs with or without DOX having a diameter <100 nm are small enough to accumulate passively via the EPR effect in the tumor region. This was clearly evident from the high-intensity fluorescence images captured from the
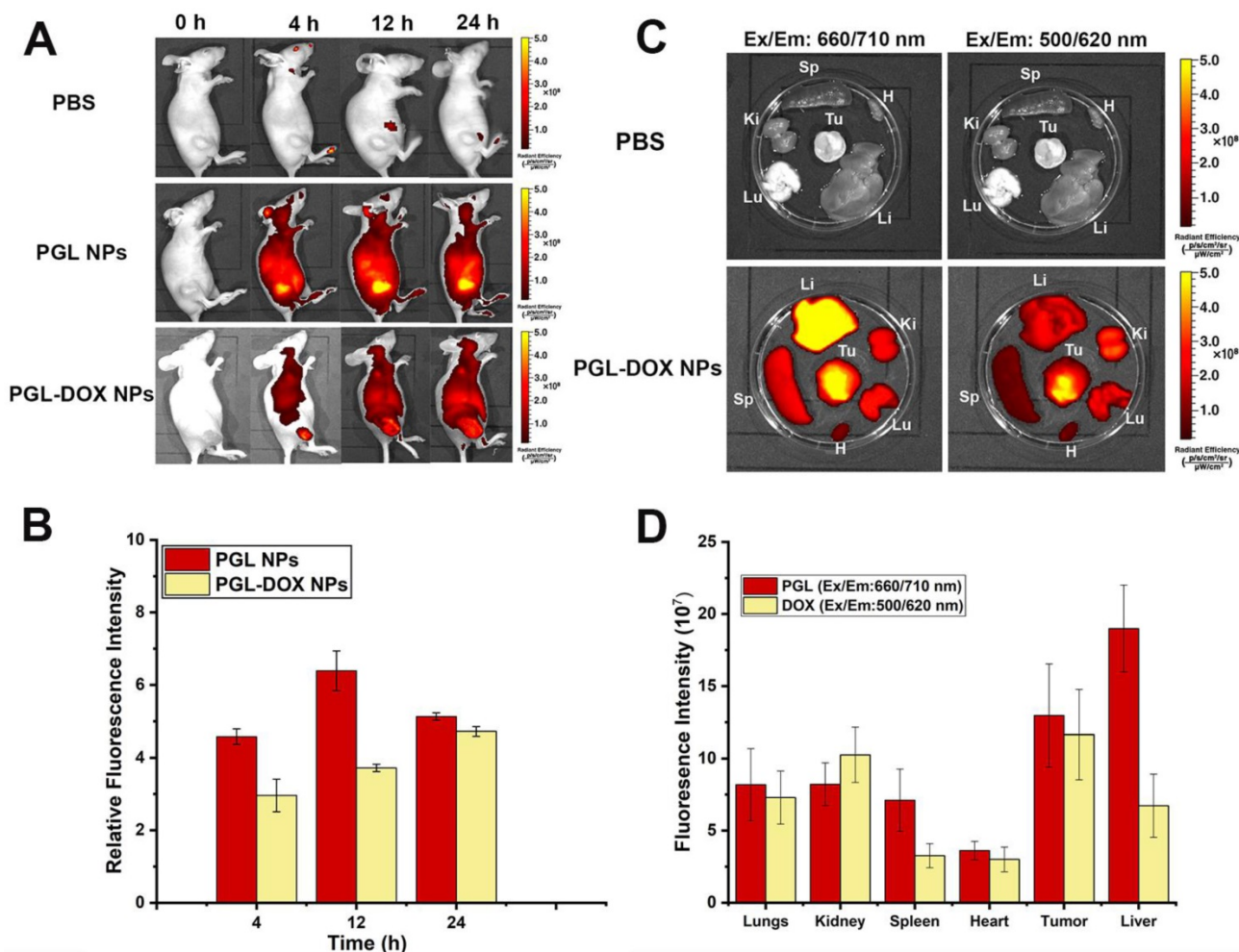

Figure 8. Biodistribution profile of PGL-DOX NPs. **(A-B)** *in vivo* fluorescence images and quantification of relative fluorescence intensity of PGL and PGL-DOX NPs in 4T1 tumor-bearing mice at 0, 4, 12 and 24 h after i.v. injection of PBS (control), PGL NPs and PGL-DOX NPs. Subcutaneous tumor sites are highlighted with a white dashed circle. **(C-D)** Ex vivo fluorescence images and quantification of fluorescence intensity of PGL-DOX NPs in various organs at 24 h determined by the fluorescence intensity of PGL (Ex/Em: 660/710 nm) and DOX (Ex/Em: 500/620 nm). The data are shown as mean ± SD.

tumor region of mice at 4 h for both PGL and PGL-DOX NPs. However, at the same molar concentration of PGL, the relative fluorescence intensity of PGL-DOX NPs was slightly lower than that of PGL NPs at different time-points. Consistent with the results of spectrophotometric analysis and *in vitro* ROS detection, we hypothesized that the π-π stacking interaction between PGL and DOX would lead to fluorescence quenching of PGL. Nevertheless, PGL NPs and PGL-DOX NPs exhibited high tumor accumulation with relatively long retention times, suggesting that the *in vivo* tumor specificities of PGL NPs and PGL-DOX NPs are greatly mediated by the EPR effect. Herein, we have also calculated and present the relative fluorescence intensities for PGL and PGL-DOX NPs *in vivo*. The fluorescence intensity 12 h after administration of PGL NPs showed the highest intensity compared to PGL-DOX NPs (**Figure 8B**). The relatively lower intensity of PGL-DOX NPs fluorescence is mainly due to the quenching effect of DOX. At 24 h post-injection, PGL NPs showed decreased fluorescence intensity *in vivo*. In contrast, PGL-DOX NPs showed relatively higher intensity even at 24 h. The observed fluorescence difference in PGL-DOX NPs could possibly be due to gradual release of DOX in the tumor region and subsequent recovery of fluorescence intensity at long time-points.

To further quantify the pharmacokinetics of the NPs, we examined the blood circulation time of PGL NPs *in vivo*. Taking into account the relatively low fluorescence intensity of PGL-DOX NPs in the tumor region compared to PGL NPs, we decided to use PGL NPs as a model to examine the blood circulation half-life. This would ensure more sensitive detection of the fluorescence signals and negate the effect of quenching from DOX. The blood circulation dynamics of PGL NPs were determined by measuring the fluorescence intensity of PGL in the plasma. The PGL signals in the plasma decreased to 42% after 8 h and only 8% was observed after 24 h (**Figure S7**). The values of elimination half-life ($t_{1/2}$) and area under the plasma concentration–time curve from 0 to 24 h (AUC_{0-24}) for PGL NPs were calculated to be 8.03 h and 827 mg h mL^{-1}, respectively.

Furthermore, to intuitively examine the biodistribution of PGL-DOX NPs, the fluorescence intensity of PGL and DOX was monitored in major organs excised from the mice (sacrificed at 24 h post-injection). As shown in **Figure 8C-D** at 24 h after intravenous administration, liver and tumor are the major organs that showed highest PGL fluorescence signals as compared to the control. In contrast, few NPs also accumulated in other organs, for instance, the signal detected from the liver was the strongest. This is a common biological challenge in which most

of the NPs gets rapidly sequestered from the blood followed by its accumulation in reticuloendothelial system (RES) organs such as liver or spleen[37].

In vivo chemo-photodynamic combination therapy

In order to evaluate the *in vivo* anti-tumor efficacy, PBS, free DOX, PGL NPs and PGL-DOX NPs (100 μL, PGL: 4.7 mg/kg, DOX: 5 mg/kg) were intravenously injected into tumor-bearing 4T1 xenograft mice (100-200 mm^3). To evaluate therapeutic efficacy, mice treated with PBS, PGL NPs and PGL-DOX NPs were irradiated with a laser (650 nm, 0.2 W/cm^2) for 30 min, 24 h post injection. As observed in **Figure S8**, the day post irradiation, mice treated with PGL and PGL-DOX NPs with laser irradiation showed slight haemorrhage at the tumor region; in contrast, mice treated with PBS plus laser had no observable injury. To evaluate the potential therapeutic outcome, tumor volume was recorded every day after different treatments. The *in vivo* study revealed a comparative therapeutic efficacy for all the treated groups post therapy. As shown in **Figure 9A**, the tumor volume rapidly increased from approximately 100 mm^3 to 800 mm^3 and 1200 mm^3 within 11 days in the PBS only and PBS plus laser treatment groups respectively, suggesting that laser irradiation was ineffective to inhibit tumor growth. On the other hand, the tumor volume of free DOX-treated mice increased from 150 mm^3 to 400 mm^3, demonstrating that free DOX alone is insufficient for suppressing tumor growth due to its non-specific tumor accumulation and short blood half-life. In the PGL NPs plus laser group, the tumor growth was largely suppressed from 150 mm^3 to 100 mm^3 in the first 6 days, after which, the tumor began to regrow and increased to a size of approximately 350 mm^3. In marked contrast, for PGL-DOX NPs plus laser-treated mice, the tumor volume was reduced to 225 mm^3. All the results confirmed that the combined PGL-DOX NPs plus laser treatment was remarkably more effective in halting the tumor growth as compared to either treatment alone. The improved therapeutic outcome of the PGL-DOX NPs-treated group is attributed to the long retention time as well as better tumor accumulation efficacy of PGL-DOX NPs. Histological sections of tumors obtained from different treatment groups also verified that the maximum damage was caused by synergistic chemo-photodynamic therapy (**Figure 9C**). Altogether, synergistic chemo-photodynamic treatment of tumor-bearing mice by using PGL-DOX NPs and laser irradiation led to significant suppression of tumor growth at 11 days post-treatment (**Figure 9D**).
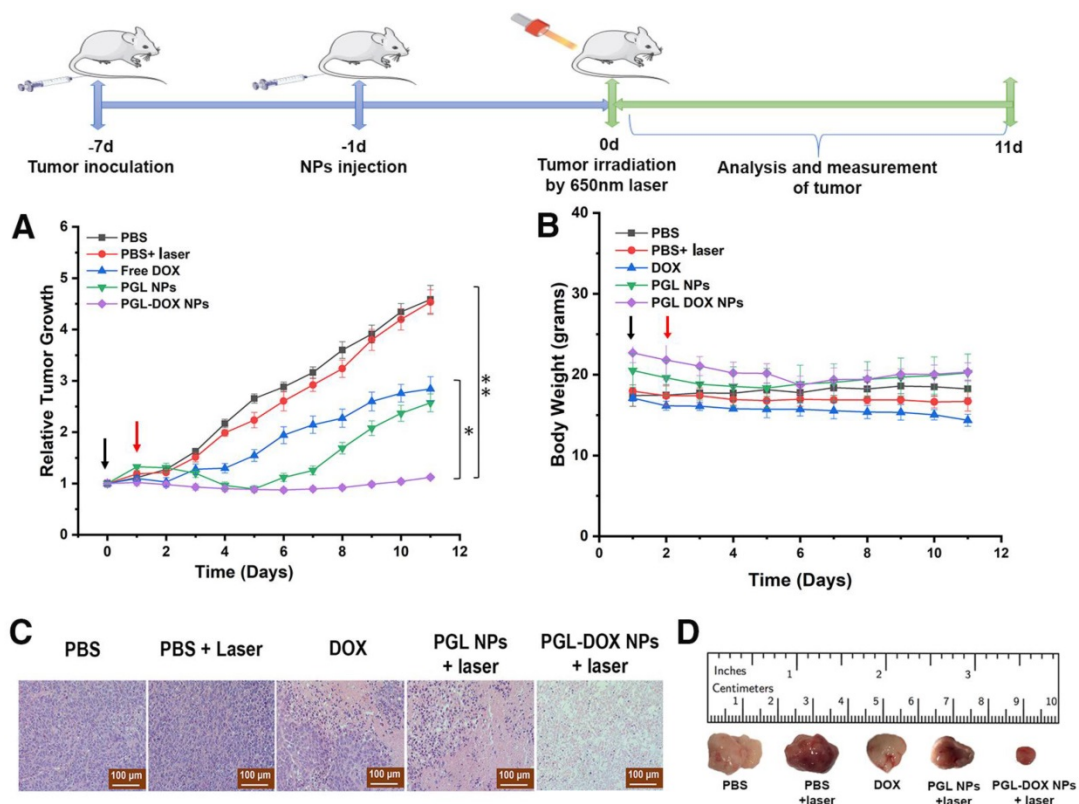
Figure 9. Tumor growth inhibition activities of different groups of mice who received various indicated treatments. PBS, free DOX, PGL NPs and PGL-DOX NPs were intravenously injected only once (indicated by the black arrow) at a DOX-equivalent dose of 5 mg/kg and PGL at an equivalent dose of 4.7 mg/kg in 4T1 tumor-bearing mice (n = 5). Mice injected with PBS, PGL NPs and PGL-DOX NPs were irradiated with 650 nm laser the next day as indicated by the red arrow. Data are expressed as mean ± SD, *$P < 0.05$, **$P < 0.01$. **(A)** Change in tumor volume, **(B)** change in body weight during the course of different treatments, **(C)** tumor histological examination by H&E staining (scale bar, 100 μm) and **(D)** photographic images of resected tumors after treatments. H&E: hematoxylin and eosin.
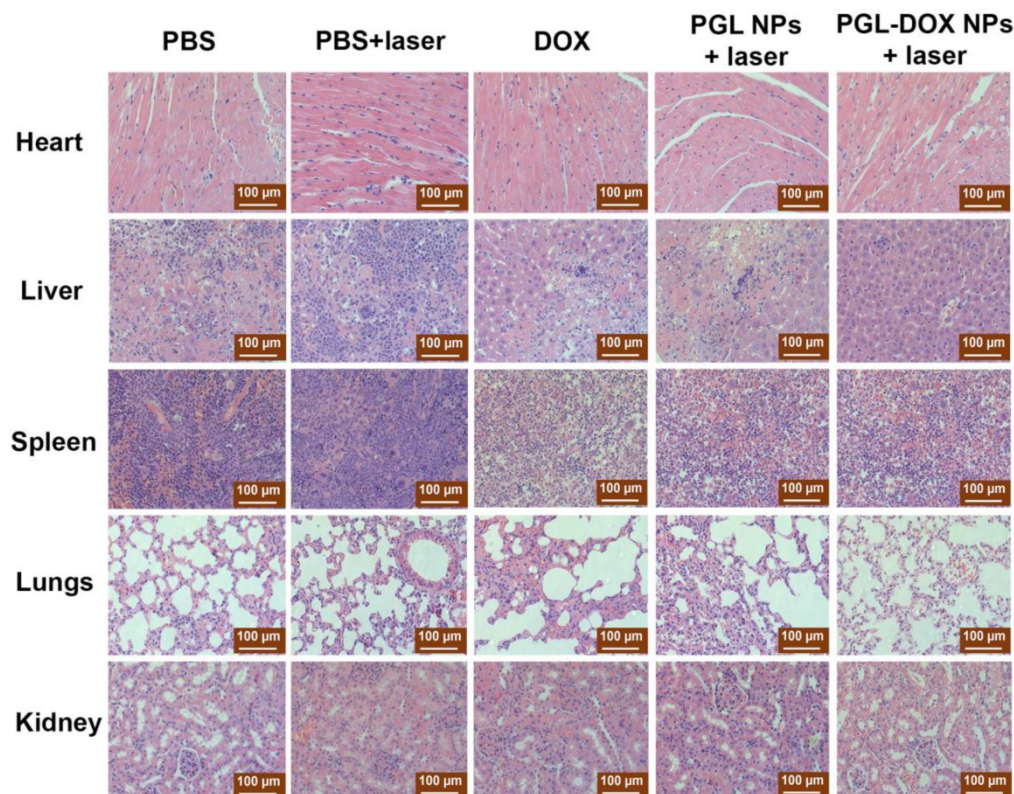

Figure 10. Representative H&E-stained microscopy images of heart, liver, spleen, lungs and kidney after different treatments (scale bar, 100 μm).

Changes in body weight of mice reflects potential toxicity caused by a particular treatment. The mouse body weight in all groups did not significantly change until the end of the treatment (**Figure 9B**). This demonstrates that PGL-DOX NPs are safe nanoformulations for chemo-photodynamic cancer therapy. Moreover, histopathological examination of vital organs (liver, spleen, kidney, and heart) with haematoxylin and eosin (H&E) staining didn't show any obvious pathological damage or lesion, suggesting that PGL-DOX NPs are extremely biocompatible without causing any evident toxicity to the major organs (**Figure 10**). All the data ensure the superiority of PGL-DOX NPs-mediated synergistic chemo–photodynamic therapy over PGL NPs alone.

Conclusion

In conclusion, a novel theranostic agent based on PGL and DOX, namely PGL-DOX NPs, was successfully developed *via* self-assembly for fluorescence imaging-guided chemo-photodynamic therapy. PGL-DOX NPs exhibited remarkably high EE, excellent stability, pH-regulated drug release, good biocompatibility and effective tumor penetration as well as retention ability. Both *in vitro* and *in vivo* experiments reflected that PGL-DOX NPs with laser irradiation showed significantly improved therapeutic activity as compared with single PDT or chemotherapy. Collectively, PGL-DOX NPs can provide a promising platform for effective diagnosis and treatment of cancer cells, which could substantially minimize the dose of chemotherapeutic DOX and improve therapeutic outcomes by fluorescence imaging-guided chemo-phototherapy.

Abbreviations

Calcein-AM: calcein acetoxymethyl ester; CCK-8: cell counter kit-8; CI: combination index; CLSM: confocal laser scanning microscopy; DLE: drug loading efficiency; DLS: dynamic light scattering; EE: encapsulation efficiency; EPR: enhanced permeability and retention; FBS: fetal bovine serum; H&E: haematoxylin and eosin; MTT: methyl thiazolyl tetrazolium; NCP: nanoscale coordinated copolymer; nDDS: nanoscale drug delivery system; OD: optical density; PBCs: porphyrin bilayer cerasomes; PDT: photodynamic therapy; PGL: porphyrin-grafted lipid; PGL-DOX NPs: porphyrin-doxorubicin nanoparticle; PI: propidium iodide; PORSILs: porphyrin-organoalkoxysilylated lipids; PS: photosensitizer; MPS: mononuclear phagocyte system; ROS: reactive oxygen species; SD: standard deviation; SOSG: singlet oxygen sensor green; TEM: transmission electron microscopy.

Supplementary Material

Acknowledgments

Competing Interests

The authors have declared that no competing interest exists.

References

1. Penteado Schmidt CW, de Menezes FG. Introduction. In: Drug therapy and interactions in pediatric oncology: a pocket guide. Cham: Springer International Publishing; 2017: 1-26.
2. Pardoll DM. The blockade of immune checkpoints in cancer immunotherapy. Nat Rev Cancer. 2012; 12: 252.
3. Gobin AM, Lee MH, Halas NJ, James WD, Drezek RA, West JL. Near-infrared resonant nanoshells for combined optical imaging and photothermal cancer therapy. Nano Lett. 2007; 7: 1929-34.
4. O'Brien MER, Wigler N, Inbar M, Rosso R, Grischke E, Santoro A, et al. Reduced cardiotoxicity and comparable efficacy in a phase III trial of pegylated liposomal doxorubicin HCl (CAELYX (TM)/Doxil (R)) versus conventional doxorubicin for first-line treatment of metastatic breast cancer. Ann Oncol. 2004; 15: 440-9.
5. Lin L, Liang X, Xu Y, Yang Y, Li X, Dai Z. Doxorubicin and indocyanine green loaded hybrid bicelles for fluorescence imaging guided synergetic chemo/photothermal therapy. Bioconjug Chem. 2017; 28: 2410-9.
6. Injac R, Perse M, Cerne M, Potocnik N, Radic N, Govedarica B, et al. Protective effects of fullerenol C-60(OH)(24) against doxorubicin-induced cardiotoxicity and hepatotoxicity in rats with colorectal cancer. Biomaterials. 2009; 30: 1184-96.
7. Cheng T, Liu J, Ren J, Huang F, Ou H, Ding Y, et al. Green tea catechin-based complex micelles combined with doxorubicin to overcome cardiotoxicity and multidrug resistance. Theranostics. 2016; 6: 1277-92.
8. Deng X, Liang Y, Peng X, Su T, Luo S, Cao J, et al. A facile strategy to generate polymeric nanoparticles for synergistic chemo-photodynamic therapy. Chem Comm. 2015; 51: 4271-4.
9. Gong H, Cheng L, Xiang J, Xu H, Feng L, Shi X, et al. Near-infrared absorbing polymeric nanoparticles as a versatile drug carrier for cancer combination therapy. Adv Funct Mater. 2013; 23: 6059-67.
10. Dougherty TJ, Gomer CJ, Henderson BW, Jori G, Kessel D, Korbelik M, et al. Photodynamic therapy. J Natl Cancer Inst. 1998; 90: 889-905
11. Kemp JA, Shim MS, Heo CY, Kwon YJ. "Combo" nanomedicine: Co-delivery of multi-modal therapeutics for efficient, targeted, and safe cancer therapy. Adv Drug Deliv Rev. 2016; 98: 3-18.
12. Han K, Wang S-B, Lei Q, Zhu J-Y, Zhang X-Z. Ratiometric biosensor for aggregation-induced emission-guided precise photodynamic therapy. ACS Nano. 2015; 9: 10268-77.
13. Dolmans DEJGJ, Fukumura D, Jain RK. Photodynamic therapy for cancer. Nat Rev Cancer. 2003; 3: 380.
14. Bulina ME, Chudakov DM, Britanova OV, Yanushevich YG, Staroverov DB, Chepurnykh TV, et al. A genetically encoded photosensitizer. Nat Biotechnol. 2005; 24: 95.
15. Liu K, Xing R, Zou Q, Ma G, Möhwald H, Yan X. Simple peptide-tuned self-assembly of photosensitizers towards anticancer photodynamic therapy. Angew Chem Int Ed. 2016; 55: 3036-9.
16. Liang X, Li X, Jing L, Yue X, Dai Z. Theranostic porphyrin dyad nanoparticles for magnetic resonance imaging guided photodynamic therapy. Biomaterials. 2014; 35: 6379-88.
17. Celli JP, Spring BQ, Rizvi I, Evans CL, Samkoe KS, Verma S, et al. Imaging and photodynamic therapy: mechanisms, monitoring, and optimization. Chem Rev. 2010; 110: 2795-838.

18. Hu J, Tang Ya, Elmenoufy AH, Xu H, Cheng Z, Yang X. Nanocomposite-based photodynamic therapy strategies for deep tumor treatment. Small. 2015; 11: 5860-87.

19. Lovell JF, Liu TWB, Chen J, Zheng G. Activatable photosensitizers for imaging and therapy. Chem Rev. 2010; 110: 2839-57.

20. Lovell JF, Jin CS, Huynh E, Jin H, Kim C, Rubinstein JL, et al. Porphysome nanovesicles generated by porphyrin bilayers for use as multimodal biophotonic contrast agents. Nat Mater. 2011; 10: 324.

21. Chauhan DS, Prasad R, Devrukhkar J, Selvaraj K, Srivastava R. Disintegrable NIR light triggered gold nanorods supported liposomal nanohybrids for cancer theranostics. Bioconjug Chem. 2018; 29: 1510-8.

22. Jin H, Dai X-H, Wu C, Pan J-M, Wang X-H, Yan Y-S, et al. Rational design of shear-thinning supramolecular hydrogels with porphyrin for controlled chemotherapeutics release and photodynamic therapy. Eur Polym J. 2015; 66: 149-59.

23. Wang H, Feng Z, Xu B. D-amino acid-containing supramolecular nanofibers for potential cancer therapeutics. Adv Drug Deliv Rev. 2017; 110-111: 102-11.

24. Hou W, Zhao X, Qian X, Pan F, Zhang C, Yang Y, et al. pH-Sensitive self-assembling nanoparticles for tumor near-infrared fluorescence imaging and chemo-photodynamic combination therapy. Nanoscale. 2016; 8: 104-16.

25. Huang F, Wang J, Qu A, Shen L, Liu J, Liu J, et al. Maintenance of amyloid beta peptide homeostasis by artificial chaperones based on mixed-shell polymeric micelles. Angew Chem Int Ed. 2014; 53: 8985-90.

26. Liu J, Yang G, Zhu W, Dong Z, Yang Y, Chao Y, et al. Light-controlled drug release from singlet-oxygen sensitive nanoscale coordination polymers enabling cancer combination therapy. Biomaterials. 2017; 146: 40-8.

27. Liao Z-X, Kempson IM, Fa Y-C, Liu M-C, Hsieh L-C, Huang K-Y, et al. Magnetically guided viral transduction of gene-based sensitization for localized photodynamic therapy to overcome multidrug resistance in breast cancer cells. Bioconjug Chem. 2017; 28: 1702-8.

28. Bacellar IOL, Tsubone TM, Pavani C, Baptista MS. Photodynamic efficiency: from molecular photochemistry to cell death. Int J Mol Sci. 2015; 16: 20523-59.

29. Liao Z-X, Kempson IM, Fa Y-C, Liu M-C, Hsieh L-C, Huang K-Y, et al. Correction to magnetically guided viral transduction of gene-based sensitization for localized photodynamic therapy to overcome multidrug resistance in breast cancer cells. Bioconjug Chem. 2018; 28: 1702-8.

30. Xiaolong L, Xiaoda L, Xiuli Y, Zhifei D. Conjugation of porphyrin to nanohybrid cerasomes for photodynamic diagnosis and therapy of cancer. Angew Chem Int Ed. 2011; 50: 11622-7.

31. Mayer LD, Bally MB, Cullis PR. Uptake of adriamycin into large unilamellar vesicles in response to a pH gradient. Biochim Biophys Acta. 1986; 857: 123-6.

32. Chen Z, Qian S, Chen X, Chen J, Zhang G, Zeng G. Investigation on the interaction between anthracyclines and DNA in the presence of paclitaxel by resonance light scattering technique. Microchim Acta. 2012; 177: 67-73.

33. Ali-Boucetta H, Al-Jamal KT, McCarthy D, Prato M, Bianco A, Kostarelos K. Multiwalled carbon nanotube-doxorubicin supramolecular complexes for cancer therapeutics. ChemComm. 2008; 0: 459-61.

34. Cao X, Tao L, Wen S, Hou W, Shi X. Hyaluronic acid-modified multiwalled carbon nanotubes for targeted delivery of doxorubicin into cancer cells. Carbohydr Res. 2015; 405: 70-7.

35. Ma L, Kohli M, Smith A. Nanoparticles for combination drug therapy. ACS Nano. 2013; 7: 9518-25.

36. Xu Y, Liang X, Bhattarai P, Sun Y, Zhou Y, Wang S, et al. Enhancing therapeutic efficacy of combined cancer phototherapy by ultrasound-mediated in situ conversion of near-infrared cyanine/porphyrin microbubbles into nanoparticles. Adv Funct Mater. 2017; 27: 1704096.

37. Yu M, Zheng J. Clearance pathways and tumor targeting of imaging nanoparticles. ACS Nano. 2015; 9: 6655-74.